A 3D full-field study of cracks in a nuclear graphite under mode I and mode II cyclic dwell loading conditions

Tim Wigger[1†], Bing Lin[1], Colin Lupton[1], James Marrow[2], Jie Tong[1]*

[1] Mechanical Behaviour of Materials Laboratory, School of Mechanical and Design Engineering, University of Portsmouth, Anglesea Building, Anglesea Road, Portsmouth PO1 3DJ, United Kingdom.

[2] Department of Materials, University of Oxford, Parks Road, Oxford OX1 3PH, United Kingdom.

*Corresponding author

Abstract

3D full-field deformation around crack tips in a nuclear graphite has been studied under mode I and mode II cyclic dwell loading conditions using Digital Volume Correlation (DVC) and integrated finite element (FE) analysis. A cracked Brazilian disk specimen of Gilsocarbon graphite was tested at selected loading angles to achieve mode I and mode II cyclic dwell loading conditions. Integrated FE analysis was carried out with the three-dimensional displacement fields measured by DVC injected into the FE model, from which the crack driving force J-integral was obtained using a damaged plasticity material model. The evolution of near-tip strains and the J-integral during the cyclic dwell loading was examined. Under cyclic dwell, residual strain accumulation was observed for the first time. The results shed some light on the effect of dwell time on the 3D crack deformation and crack driving force in Gilsocarbon under cyclic mode I and II loading conditions.

1. Introduction

[†] Now at Department of Mechanical Engineering, UCL, London WC1E 7JE, United Kingdom

Polygranular graphite components, used in Advanced Gas cooled Reactors (AGRs) as moderator and structural components in the reactor core, are required to withstand variable stresses from a number of sources, including thermal gradients, irradiation and pressure fluctuations of the gas coolant during routine operational cycles of reactors.[1,2] The strength of graphite depends on the extension of inherent flaws in its structure,[1,3,4] so knowledge of the fracture behaviour of nuclear graphite has been recognised to be of critical importance for the safe and reliable operation of these reactors. High confidence in the properties of the reactor components is required for the AGR reactors that remain in service after exceeding their designated lifetime,[5] also future high temperature reactors with graphite components in their core[6,7] for which design against the effects of thermal fatigue loading is an additional concern.

Fracture behaviour in nuclear graphite has been studied using a wide range of experimental methods, including Computed Tomography (CT)[8] together with Digital Image Correlation (DIC),[9,10] Digital Volume Correlation (DVC)[11–13] as well as neutron and synchrotron X-ray diffraction[14] and finite element (FE) analysis.[15–17] Various mechanical parameters including the stress intensity factor, T stress, strain energy release rate, J integral and R curve have been utilised to quantify fracture behaviour, and a range of experimental studies have been carried out at both macro[9] and micro scales[8–11] to obtain information on crack nucleation, steady-state crack growth and crack bridging and other attenuation mechanisms. The fracture behaviour of coarse grained polygranular graphite, such as the Gilsocarbon used in the UK's AGRs, has been shown to be determined by the propagation of pre-existing defects in the microstructure.[13,18] Non-irradiated graphite has non-linear behaviour and also develops non-recoverable strains,[14] which may occur via crystal deformation mechanisms and/or microcracking. X-ray tomography of a propagating macroscopic crack in non-irradiated graphite has revealed a microcracked fracture process zone,[19] with nonlinear properties that influence the crack opening behaviour.[20] The fracture process zone can be simulated with a cohesive model,[20,21] with elastic properties verified[11] by *in situ* neutron and X-ray strain mapping with image correlation.[14] The influence of temperature on strength and toughness[12] and crack arrest[22,23] have been examined; whilst numerical simulations have been carried out to examine irradiation-induced creep[15] and also the effects of temperature on crack propagation[16] and stress distributions.[17]

2

Most of the previous work considered mode I cracks, although flaws in graphite are not necessarily straight or ideally oriented perpendicularly to the loading direction. Kinked or branched cracks are observed in the microstructure,[11,24,25] and crack growth has been found to deviate from the original crack plane, either due to the brick geometry[23] or the complex stress states that develop at increased irradiation dose levels.[16] A few studies of fracture from notches have been carried out under mode II[26,27] and mixed mode[28,29] loading conditions, and the notch sensitivity of graphite has also been investigated using a strain energy density approach.[28,29] Some early studies[3,30–33] have reported fatigue crack growth and fatigue lives of nuclear graphite. However, these offer limited insight into the material behaviour during crack growth under cyclic loading conditions, mainly due to the limitations in the methods of studies in the past. The material behaviour near a crack tip in a nuclear graphite has not been quantitatively studied before, particularly under cyclic dwell conditions and in mode II.

In this work, a Brazilian disc specimen was utilised to achieve cyclic mode I and mode II loadings. Pre-cracks were introduced under static compression first, and cyclic experiments followed with the specimen tested at two loading angles, and imaged, *in situ,* using a microCT scanner. 3D images of the specimen were collected at selected load cases, from which digital volume correlation (DVC) was carried out to obtain the full-field displacements and strains. Hold periods were introduced at the peak load of a cycle to examine the effects of dwell loading on the development of the near-tip strains at zero and peak loads. The experiments were complemented by an integrated FE, where the measured displacements from the DVC were injected into the FE model as boundary conditions, and a standard FE analysis. A damaged plasticity material model, calibrated to graphite material, was used in the FE analyses to obtain further micro-mechanics information and to compute the crack driving force J-integral.

2. Experimental Procedures

2.1 Material and Specimen

The nuclear graphite studied in this work is virgin (non-irradiated) Gilsocarbon. The material consists of near-spherical Gilsonite coke particles with an average diameter of 500 μm in a matrix of pitch and fine coke particles, resulting in a structure with approximately 20%

3

porosity after moulding and graphitisation at up to 2700°C.[34] The graphite is essentially isotropic (isotropy ratio 1.04), has an elastic modulus of around 11 GPa and a Poisson's ratio of 0.2.[34] Unlike fast-neutron irradiated nuclear graphite, which can be characterised essentially as linear-elastic, the present non-irradiated Gilsocarbon shows non-linear mechanical behaviour.[9,14,35]

A Brazilian disc specimen was used for all experiments in the present study to achieve mode I and mode II loading conditions by changing the angle α between the load direction and the crack plane (Figure 1A). The specimen has a diameter of 20 mm and a thickness of 9 mm. A through-thickness notch of 4 mm in length and 0.3 mm in width was produced by electrical discharge machining from a centre hole of 2 mm diameter (Figure 1A), where the U-shaped tips of the notch have a radius of 150 μm. The notch tips were then sharpened with a razor blade to facilitate crack initiation.

2.2 Pre-cracking

Pre-cracking was carried out on an MTS testing machine with a 15 kN load cell. The specimen was progressively loaded in compression, with the notch oriented parallel to the loading direction (α = 0°) until cracks formed from the notch tips. The process was monitored optically. Aluminium saddles (Figure 1B) were employed to increase the contact areas during pre-cracking to prevent local damage to the specimen edge during compression. Cracks initiated from the notch tips at around 5000 N (Figure 1C), corresponding to approximately a stress intensity factor of K_I of 1.5 MPa√m, which is consistent with the reported fracture toughness of 1.3 MPa√m for Gilsocarbon.[9]

2.3 Crack geometry

To determine the precise crack geometry, the sample was subjected to a load of 1600 N to keep the crack faces open at α = 0°, and scanned using a Nikon/Metris micro-computed-tomography (μCT) system. Volumetric images of around 1000 x 1000 x 800 voxels[3] with a spatial resolution of approximately 25 μm per voxel were produced; and the crack lengths across the specimen thickness were measured directly from the tomographs (Figure 2A). In this specimen, the observed length ranged from 1.2 mm in the centre to 2.3 mm on the surfaces of the specimen (Figure 2B). The artificial sharpening of the surfaces of the notch

tips and the lack of significant plastic deformation near the surfaces may be responsible for the longer crack lengths near the surfaces.

2.4 Loading arrangement

The specimen was loaded in either mode I or mode II by changing the loading angle α (Figure 1A). The load levels were determined to ensure no macro-crack growth during cyclic testing, based on information on fatigue threshold of the material.[31] The stress intensity factor for mode I and mode II may be calculated by:[36]

$$K_I = \frac{P}{B\sqrt{R_d}} Y^{\square}$$

(1)

Where P is the applied load, B the specimen thickness and R_d the specimen radius. The parameter Y is a geometry factor that may be solved for pure mode I, Y_I, and mode II, Y_{II}, conditions:

$$\begin{aligned} Y_I = {} & 0.0354 + 2.0394\chi - 7.0356\chi^2 + 12.8154\chi^3 + 8.4111\chi^4 \\ & - 30.7418\chi^5 - 29.4959\chi^6 + 62.9739\chi^7 + 66.5439\chi^8 \\ & - 82.1339\chi^9 - 73.6742\chi^{10} + 73.8466\chi^{11} \end{aligned}$$

(2)

$$\begin{aligned} Y_{II} = {} & 0.06462 + 2.8956\chi - 6.8663\chi^2 + 9.8566\chi^3 - 0.4455\chi^4 \\ & - 1.0494\chi^5 - 13.2492\chi^6 + 9.0783\chi^7 - 10.7354\chi^8 \\ & + 28.4775\chi^9 - 6.3197\chi^{10} + 10.6626\chi^{11} - 10.0268\chi^{12} \\ & - 34.2997\chi^{13} + 1.7292\chi^{14} + 25.2216\chi^{15} \end{aligned}$$

(3)

Where $\chi = a/R_d$, and the radius of the disc, R_d, is 10 mm. Mode I is achieved at $\alpha_I = 0°$; whilst pure mode II is achieved at $Y_I = 0$. The angle α_{II} is a function of $\chi = a/R_d$:

$$\begin{aligned} \alpha_{II} = {} & 30.4406 - 4.6734\chi - 17.6741\chi^2 - 9.6827\chi^3 + 3.9819\chi^4 \\ & + 12.9163\chi^5 - 13.3222\chi^6 + 12.8001\chi^7 - 13.1239\chi^8 \end{aligned}$$

(4)

for a = 3.55 mm, with an average crack length of 1.6 mm from the notch tip and a half notch length of 1.95 mm, $\alpha_{II} \approx 27°$. The maximum load for the cyclic testing was chosen to be 1800N, with the resulting of maximum mode I stress intensity factor (0.8 MPa√m) and its range (R=0) below the fracture toughness (1.3 MPa√m[9]) and the fatigue threshold (0.85 MPa√m [31]).

2.5 Mechanical testing

Cyclic tests were carried out post pre-cracking, with the specimen mounted inside a microCT scanner (Nikon XTH-225 X-ray & CT Inspection System) at Portsmouth, and loaded *in situ* with a screw-driven loading stage (Deben Ltd., UK). The pre-cracked specimen was first loaded for 10 cycles in mode I at a peak load 1800 N (R=0), with no hold at the peak loads, and tomography scans were recorded after each cycle at zero load. The effect of dwell on the near-tip deformation was then examined, with a hold period of 90 and 120 mins, respectively, introduced at the peak loads (1800 N) in mode I (R=0) for six cycles. Tomographs were recorded during the hold periods and also after unloading at zero load for each cycle. In mode II, a total of ten cycles were applied, with a hold period of 90 minutes introduced at peak loads (1800 N). Tomographs were recorded during the hold periods and at zero load post unloading. CT scanning was carried out at 170 kV and 110 μA, with a spatial resolution around 25 μm / voxel at 16 bit. A total of 3600 projections across 360° was obtained over a duration of 60 minutes for each scan. The objective was to capture 3D full-field deformation and its evolution near the crack tips *in situ*, with a particular interest in the role of cyclic dwell.

2.6 Digital volume correlation (DVC)

DVC was carried out on all volumes reconstructed from the scanned images by correlating those obtained under loads with a zero-load reference volume to extract three dimensional full-field deformation.[37] This method tracks the pattern shifts in discretised "subvolume" elements of the volumetric images to generate a 3D-grid of displacement vectors. The software DaVis 10 (LaVision GmbH) was used in this work. The displacements of subvolumes with a size of 32^3 voxels^3 (800^3 μm^3) were tracked on a grid with 16 voxels (400 μm) distance (i.e. 50% overlap). The displacement field for the whole volume was then bi-cubically interpolated to obtain a vector grid with a resolution of 4 voxels (100 μm).

After volume correlation was completed, strain maps were derived from the displacement data by computing the x- and y-gradients within 3x3 data points around each grid position. The precision of the procedure was determined by correlating the reference image with a rigid body translated image and measuring the resulting standard deviation of displacements and strains in the field. The average strains normal to the crack plane (ε_{xx}) and the average shear strains (ε_{xy}) at selected locations (0.3, 0.6, 0.9 mm ahead of the crack front) were

determined in a measurement volume of 0.2×0.2×0.8 mm^3 along the perceived planar crack plane.

3. Finite Element Analysis

3.1 The FE model

A FE model was created for the same geometry of the Gilsocarbon specimen as used in the experiment (**2.1**). The commercial software ABAQUS[38] was used to carry out both a *standard* and an *integrated* FE analysis. The actual crack front profiles captured from the tomography, as shown in Figure 2(B), were introduced into the 3D FE model. For the standard analysis (Figure 3A), the loads were applied via two rigid surfaces between which the specimen was rotated to achieve mode I and mode II loading conditions. Contact pairs were defined between the rigid surface and the specimen surface to prevent their potential overlapping in the FE simulation (Figure 3A). For the integrated FE analysis (Figure 3B), the displacements from the DVC were injected as the boundary conditions.[39] The mesh size around the crack was chosen so that the nodal spacing of the FE mesh matched the DVC grid size of 0.4 mm, hence the two grids between the DVC and the FE model are consistently registered. A mesh convergence analysis was conducted and the mesh size of 0.4 mm was found to be adequate in capturing the crack tip deformation. To reduce the effects of image noise due to the discontinuity of the crack on the calculation of the J-integral, a region free of the DVC displacement data around the crack was built in the FE model[39] (Figure 3B). To prevent element volumetric locking during the FE analysis, an eight-nodded element (C3D8R) with reduced integration was chosen to mesh the model. The total numbers of elements and nodes in the FE model are 49736 and 54314, respectively. The crack was assumed stationary and no crack growth was simulated. The frictional effects between the crack flanks were ignored.

3.2 The material model

Experimental studies[11] of un-irradiated Gilsocarbon have shown that crack propagation occurred within a fracture process zone (FPZ), where micro-cracking caused a tensile strain-dependent decrease in elastic modulus. This has been confirmed by X-ray and neutron diffraction measurements of stress in virgin Gilsocarbon that was strained in tension, flexure and compression.[14] The choice of an appropriate material model depends on the ratio of a

7

structural size D, such as the uncracked ligament in the specimen, and the fracture process zone length l_{ch}.[40] In the present study, $D/l_{ch} < 5$, hence a non-local material model,[40] Concrete damaged plasticity (CDP), available in ABAQUS,[38] was utilised in the FE analysis, following previous work on the same material.[41]

In the CDP model, a modified yield function of Lubliner et al.[42] is used, in which different deformation behaviour in tension and compression was considered. The hardening variables, $\tilde{\varepsilon}_t^{pl}$ and $\tilde{\varepsilon}_c^{pl}$, control the yield surface's evolution, and the yield function takes the following form:

$$F = \frac{1}{1-\alpha}(\bar{q} - 3\alpha\bar{p} + \beta\tilde{\varepsilon}^{pl} < \hat{\bar{\sigma}}_{max} > -\gamma < -\hat{\bar{\sigma}}_{max} >) - \bar{\sigma}_c(\tilde{\varepsilon}_c^{pl}) \leq 0 \qquad (5)$$

where $\bar{p}$ is the effective hydrostatic pressure; $\bar{q}$ is the Mises equivalent effective stress; $\hat{\bar{\sigma}}_{max}$ is the maximum principal effective stress; $\tilde{\varepsilon}^{pl}$ is characterised by two hardening variables, $\tilde{\varepsilon}_t^{pl}$ and $\tilde{\varepsilon}_c^{pl}$, which are referred to as equivalent plastic strains in tension and compression.

The non-associated potential flow is assumed, and the Drucker-Prager hyperbolic function is used in the CDP model, so the flow potential G is written as:

$$G = \sqrt{(\epsilon\sigma_{t0}tan\psi)^2 + \bar{q}^2} - \bar{p}tan\psi \qquad (6)$$

where σ_{t0} is the uniaxial tensile failure stress; ψ is the dilation angle measured in the $p - q$ plane under high confining pressure; ϵ is an eccentricity parameter by which the rate of the function approaching the asymptote is defined.

The fracture energy G_f is used to define the post-yield tensile behaviour in the CDP model. By specifying the post-failure stress as a function of cracking displacement u_t^{ck}, the cracking model based on the G_f can be invoked. The plastic displacement at cracking may be assumed as:

$$u_t^{pl} = u_t^{ck} - \frac{d_t}{(1-d_t)}\frac{\sigma_t l_0}{E_0} \qquad (7)$$

where d_t is tensile damage and the specimen length l_0 is assumed to be one unit length. For compressive deformation plastic strain may be obtained from inelastic strain $\tilde{\varepsilon}_c^{in}$:

$$\tilde{\varepsilon}_c^{pl} = \tilde{\varepsilon}_c^{in} - \frac{d_c}{(1-d_c)}\frac{\sigma_c}{E_0} \tag{8}$$

where d_c and σ_c are scalar compressive damage variable and compressive stress, respectively.

The stress-strain relation of the viscoplastic model is given as:

$$\sigma = (1 - d_v)D_0^{el}:(\varepsilon - \varepsilon_v^{pl}) \tag{9}$$

where d_v is a viscous stiffness degradation variable, and D_0^{el} is the initial (undamaged) elasticity matrix. ε_v^{pl} is the viscoplastic strain. The time-dependency of the model is expressed in the visco-plastic strain rate, $\dot{\varepsilon}_v^{pl}$:

$$\dot{\varepsilon}_v^{pl} = \frac{1}{\mu}\left(\varepsilon^{pl} - \varepsilon_v^{pl}\right) \tag{10}$$

where μ is a time-dependent viscosity parameter, which was obtained by matching the results of normal strain vs cycle for the 90 min hold from the standard and the integrated FE analysis, with an initial value of μ = 0.0005 for concrete[43] to begin with. The viscosity parameter was estimated to be μ = 0.0003 and applied in all the FE simulations. The rest of the model parameters used were taken from a previous study[41] on the modelling of Gilsocarbon graphite using the CDP model, and are summarised in Table 1.

4. Results

4.1 Near-tip strain evolution

Stationary cracks were assumed (**2.4**), and this was confirmed by the experiments as no crack growth was detected optically during scanning, or from the tomography reconstruction post scanning. The same crack geometry was used for all experiments and simulations. The normal and shear strains were obtained at three positions: 0.3, 0.6, 0.9 mm ahead of the crack front along the perceived planar crack path, as shown in Figure 2. The average strain values were taken in a volume of $0.2{\times}0.2{\times}0.8$ mm^3, and the standard deviation of the strain measurement is about 0.04%. The reference strain value was taken at zero load before each cycle in the experiments.

The residual strains upon unloading were assessed at zero load for a hold period of 0, 90 and 120 mins, and the results are presented in Figure 4. Without hold, the strains in the

unloaded state after each cycle were found to be negligible, within a scatter band of ±0.02%. For a dwell period of 90 mins, notable increase in residual strains is observed, albeit with significant scatters. Significant increase in the residual strains is evident for a dwell period of 120 mins, where within the limited six cycles residual strains up to 0.24% are observed. It seems that the increase of dwell period prompts the development of the residual strains.

The evolution of the normal strains under mode I cyclic loading is presented in Figure 5 for a hold period of (A) 90 mins and (B) 120 mins at the maximum and the minimum (zero) loads. The strains were tracked at three positions ahead of the crack tip, with the reference value taken at zero load. The results from the standard FE simulation are also included for comparison. The normal strains at the maximum load increased with cycles in all three tracking points for both cases, although more pronounced at the longer dwell time. For case A at 90 mins dwell, the strain increased from 0.23% at cycle 1 to 0.30% at cycle 6 at a distance of 0.6 mm to the crack front (Figure 5A); whilst the residual strains at zero load increased slightly, up to 0.11% at the same tracking position with some scatters. The standard FE results at this position seem to be consistent with the experimental measurements, increasing with cycle from 0.2% to 0.33% at the maximum; and from zero to 0.08% at zero load. At longer dwell time of 120 minutes (Figure 5B), the increase in normal strains with cycle is more evident at all tracking positions, up to 0.39% at a distance of 0.6 mm to the crack front at the maximum load. The increase in the residual strains at zero load is also more notable in all tracking positions, up to 0.18% at a distance of 0.6 mm to crack front. The normal strains simulated by the standard FE analysis show a similar trend, up to 0.41% at maximum load; and up to 0.09% at zero load at the same location (Figure 5B).

The near-tip shear strains were tracked at the selected locations to the crack front at both maximum and minimum loads post unloading, as in mode I; and the results are shown in Figure 6. It appears that the shear strains at P_{max} remain almost constant around 0.40% during the first 3 cycles and increased very slightly to approximately 0.45% during cycle 4, after which the strains remained unchanged during further cycles. Upon unloading, the residual shear strains appear to increase slightly with cycle, up to 0.09% within 10 cycles, although these results are likely to be affected by the strain measurement uncertainty of ±0.02%. The shear strains are predicted to increase steadily in the standard FE analysis, and the shear strain at the maximum load is predicted to increase up to 0.50% over 10 cycles at a

10

distance of 0.6 mm to the crack tip. In the unloaded state, the predicted residual shear strains also increased steadily up to 0.07% at the same location. The discrepancies between the experimental measurements and those of FE simulation may be due to the possible interlocking between the crack surfaces under mode II loading in the experiment, as opposed to idealised crack surfaces assumed in the FE simulation. It is plausible that the variation in the shear strains measured by DVC is reflective of the relative motions or lack of them due to local surface conditions. Surface interlocking is known to affect shear stresses in quasi-brittle materials.[44] As opposed to mode I, there seems to be very limited increase in the measured shear strains in mode II as a result of cyclic dwell loading. Admittedly, the model was calibrated against the experimental data obtained from mode I,[41] hence the predicted time-dependent behaviour is not dissimilar to that of mode I whilst physical deformation mechanisms in mode II, such as interlocking, could not be simulated.

4.2 Crack driving force

The effect of cyclic dwell loading on the J-integral as a crack driving force was assessed. Both standard FE and integrated FE analyses were carried out in mode I and mode II for the sustained periods as in the experiments. The values of the J-integral at zero load (P_0) were obtained at each cycle after unloading, following a sustained period at the peak load; whilst J values were also obtained for each cycle at the peak load after the sustained period. Full 3D calculations were carried out, and the values of J were measured across the entire crack front from both standard FE (denoted as FE) and integrated FE (denoted as DVC). The results are shown in Figure 7 for the case of mode I with a 90 min dwell period at minimum load (A) and maximum load (B); and 120 min dwell period at minimum load (C) and maximum load (D).

Generally, the results from the integrated and standard analysis are not dissimilar, and the broad trends are the same for both dwell loading cases. The values of J are higher near the surfaces of the specimen than that in the interior, by approximately 70% to 200% at P_0 and 30% to 80% at P_{max}. The effects of dwell loading on J at zero load appear to be insignificant (Figure 7A, C). There are some differences in the values of J at P_0 for the longer dwell period (120 min), where the actual values of J from the integrated analysis on the surfaces are notably higher (around 50%) than those predicted using the standard analysis. At the maximum loads, however, the effects of dwell loading on J are significant, with the values of J increase by 30% to 150% relative to those at cycle one from both standard and integrated

11

FE analyses. Post dwell cyclic loading, the differences in the values of J near the surface and in the interior become more evident, varying from 30% to 80%.

Under mode II loading, the differences between the values of J near the surfaces and in the interior appear to be small (Figure 8A), although the effects of dwell on the J-integral are significant (Figure 8B). Both standard FE and integrated FE produce similar results, in that the values of J at peak load at cycle ten are about double of those at cycle one (Figure 8B).

5. Discussion

In this work, the near-tip behaviour of Gilsocarbon graphite has been studied in 3D under cyclic dwell loads for the first time, using both *in situ* experiments and FE simulations. Cracks in quasi-brittle materials are known to propagate due to the formation and the growth of micro-cracks in a fracture processing zone (FPZ) ahead of the crack tip, leading to a non-linear stress-strain response and softening behaviour post the peak stress. The effects of cyclic dwell loading on the near-tip strain development and the crack driving force, as measured using the J-integral, have been studied in mode I and mode II in this material, using a non-local damage plastic model.[38,40,41] A progressive increase in normal strains (Figure 5) at both minimum and maximum loads is evident, particularly at locations close to the crack tip and for long dwell periods. The results clearly show that the accumulation of non-reversible deformation, or strain ratchetting, is significant. This phenomenon is known to be relevant to fatigue crack growth in ductile metals,[45,46] it is interesting to note that it also occurred in quasi-brittle polygranular graphite. A combined action of cyclic and dwell loading is believed to be at work in promoting the deformation, although the role of cycling appears to be limited due to the small number of cycles examined. Dwell duration, on the other hand, seems to play a dominant role in the development of normal strains in the present cases.

Nuclear graphite can undergo time-dependent deformation by thermal creep[47] at temperatures beyond 2000°C and irradiation-induced creep.[34] Although these mechanisms are not relevant here, a previous study[48] using nano-indentation revealed residual deformation upon unloading in virgin IG110 and PGA nuclear graphite grades at room temperature. Possible underlying mechanisms may be basal plane slip in the graphite crystals or progressive initiation and interconnection of microcracks, common in quasi-brittle materials.[49]

12

Unlike mode I, the link between shear strain development and cyclic dwell loading appears to be weak from the experimental measurements (Figure 6), although residual strains still present. Both shear strains at maximum and minimum loads appear to be relatively stable, which may be due to local microstructural characteristics such as interlocking/bridging.[10–12,44] It seems that after the first loading in mode II, the surfaces were "locked" in place till cycle 4, when a marginal increase in shear strain was observed. Such behaviour appears to be consistent with a previous report,[36] where residual "opening" was found in cracks in Gilsocarbon after mode I cycles, probably due to surface roughness. Such behaviour cannot be predicted from the FE analysis, as microstructural characteristics pertinent to mode II deformation cannot be simulated. The FE model assumed idealised crack surfaces and the model parameters were obtained from the mode I experiments, hence the predicted trend of strain accumulation is broadly similar to that under mode I.

The crack driving force in terms of J-integral has been examined across the thickness of the specimen, at minimum and maximum loads. Both standard FE and integrated FE analysis were carried out, and the results seem to be consistent. The effects of thickness appear to be most evident for mode I at minimum loads (Figure 7A, C), and post a long dwell period (Figure 7B, D), with the values of J near the surfaces more than doubled the initial values of J post cycling, particularly at 120 min dwell (Figure 7D). Lower constraints and longer cracks near the specimen surfaces permit greater deformation, hence higher J-integral values are obtained. This is consistent with the observation from previous studies.[50,51] However, the effect of thickness seems not apparent under mode II loading conditions (Figure 8A).

In both mode I and mode II, significantly elevated J values were obtained post cyclic dwell loading (Figure 7B, D; Figure 8B) at peak loads. The standard FE simulations appear to produce broadly similar results to those from the integrated analysis using DVC data, albeit with more scatters. This seems to suggest that there is little "attenuation" effect in the actual strain evolution or crack driving force at this relatively low loading level. It is possible that at higher loads, some of the stress shielding effects observed during fracture tests [9-12] might play some roles in the damage development.

The J-integral was calculated from the data collected from DVC under the assumption of a stationary crack with a fixed crack tip position. This hypothesis appears to be true as no crack growth was detected optically during scanning, or from tomography reconstruction post

13

scanning. Considering that both the maximum and the range of stress intensity factor of the cyclic experiments are below the fracture toughness[9] and the fatigue threshold for reactor graphites[31], crack propagation seems to be unlikely.

The formation of microcracks in graphite may be accelerated by environmental factors, such as stress corrosion from atmospheric moisture. Higher water contents in the surrounding atmosphere are known to reduce the strength of nuclear graphite,[52] and it is a recommended practice to reduce the water content by "baking" samples before fracture toughness testing.[53] Microcracking in the fracture process zone due to local tensile stresses may be facilitated by the exposure to the environment, partcularly near the surfaces, which may have elevated the crack tip strains in these areas. In mode II, on the other hand, the lack of local tensile stresses might help to explain the lack of variation in strains and J across the thickness. A closer examination of the micro-mechanisms responsible for the strain accumulation phenomenon in graphite would be helpful for developing materials with improved damage resistance.

A non-local damage plastic model[38,41] has been used to predict and simulate the full-field near-tip mechanical responses under cyclic dwell loading conditions in mode I and mode II. Admittedly, most of the model parameters were estimated from a previous mode I experiment,[41] and the post yield modulus reduction was not considered in the model. Surface characteristics were not simulated for mode II loading. These aspects may be explored in future work, with the present study as a baseline, under more complex loading, temperature and irradiation conditions.

6. Conclusions

The full-field deformation ahead of a 3D crack front in a Brazilian disc of Gilsocarbon graphite has been examined by *in situ* CT under cyclic dwell loading conditions in mode I and mode II. Integrated FE and standard FE analyses were carried out to obtain the near-tip strains and to compute the J-integral. Dwell time superimposed at the peak cyclic loads appears to promote the development of residual strains at zero load and strain accumulation at the peak loads in mode I, although the effects seem to be less pronounced for mode II. Furthermore, the crack driving force measured in J-integral increases significantly when a hold period is superimposed on the peak load for both mode I and mode II. Further studies of the near-tip

14

damage mechanisms under cyclic dwell loading conditions may help to gain a physical understanding towards the formulation of a predictive tool in the damage tolerance management of graphite reactor components for long-term safe operation of AGR.

Acknowledgements:

References

1   Maul P, Robinson P, Burrow J, Bond A. Cracking in Nuclear Graphite. *Math Today*. 2017: 116–119.

2   Tsang DKL, Marsden BJ. The development of a stress analysis code for nuclear graphite components in gas-cooled reactors. *J Nucl Mater*. 2006;350: 208–220.

3   Ishiyama S, Oku T, Eto M. Fatigue failure and fracture mechanics of graphites for high temperature engineering testing reactor. *J Nucl Sci Technol*. 1991;28: 472–483.

4   Karthik C, Kane J, Butt DP, Windes WE, Ubic R. Microstructural Characterization of Next Generation Nuclear Graphites Microstructural Characterization of Next Generation. *Microsc Microanal*. 2012;18: 272–278.

5   WNN. EDF Energy extends lives of UK AGR plants. *World Nuclear News*. 2016.

6   Sumita J, Shimazaki Y, Shibata T. Investigation on structural integrity of graphite component during high temperature 950 ° C continuous operation of HTTR. *J Nucl Sci Technol*. 2014;51: 1364–1372.

7   Mohanty S, Majumdar S, Srinivasan M. Constitutive modeling and finite element procedure development for stress analysis of prismatic high temperature gas cooled reactor graphite core components   . *Nucl Eng Des*. 2013;260: 145–154.

8   Marrow J, Hodgkins A, Joyce M, Marsden BJ. Damage nucleation in nuclear graphite. *Energy Mater Mater Sci Eng Energy Syst*. 2006;1: 167–170.

9   Becker TH, Marrow TJ, Tait RB. Damage, crack growth and fracture characteristics of nuclear grade graphite using the Double Torsion technique. *J Nucl Mater*. 2011;414: 32–43.

10   Mostafavi M, Marrow TJ. Quantitative in situ study of short crack propagation in polygranular graphite by digital image correlation. *Fatigue Fract Eng Mater Struct*. 2012;35: 695–707.

11   Barhli SM, Saucedo-Mora L, Jordan MSL, et al. Synchrotron X-ray characterization of crack strain fields in polygranular graphite. *Carbon N Y*. 2017;124: 357–371.

12   Liu D, Gludovatz B, Barnard HS, Kuball M, Ritchie RO. Damage tolerance of nuclear graphite at elevated temperatures. *Nat Commun*. 2017;8: 1–9.

13   Mostafavi M, McDonald SA, Çetinel H, Mummery PM, Marrow TJ. Flexural strength and defect behaviour of polygranular graphite under different states of stress. *Carbon N Y*. 2013;59: 325–336.

14   Marrow TJ, Liu D, Barhli SM, et al. In situ measurement of the strains within a mechanically loaded polygranular graphite. *Carbon N Y*. 2016;96: 285–302.

15   Fang X, Wang H, Yu S, Li C. The various creep models for irradiation behavior of nuclear graphite. *Nucl Eng Des*. 2012;242: 19–25.

16   Wadsworth M, Kyaw ST, Sun W. Finite element modelling of the effect of temperature and neutron dose on the fracture behaviour of nuclear reactor graphite bricks. *Nucl Eng Des*. 2014;280: 1–7.

17   Hashim A, Kyaw S, Sun W. Modelling fracture of aged graphite bricks under radiation and temperature. *Nucl Mater Energy*. 2017;11: 3–11.

18   Joyce MR, Marrow TJ, Mummery P, Marsden BJ. Observation of microstructure deformation and damage in nuclear graphite. *Eng Fract Mech*. 2008;75: 3633–3645.

19   Hodgkins A, Marrow TJ, Mummery P, et al. X-ray tomography observation of crack propagation in nuclear graphite. *Mater Sci Technol*. 2006;22: 1045–1051.

20   Mostafavi M, Baimpas N, Tarleton E, et al. Three-dimensional crack observation, quantification and simulation in a quasi-brittle material. *Acta Mater*. 2013;61: 6276–6289.

21   Chen HHN, Su RKL, Fok SL, Zhang HG. Fracture behavior of nuclear graphite under three-point bending tests. *Eng Fract Mech*. 2017;186: 143–157.

16

22   Singh G, Fok A, Mantell S. Failure Predictions for Graphite Reflector Bricks in the Very High Temperature Reactor with the Prismatic Core Design. *Nucl Eng Des*. 2017;317: 190–198.

23   Treifi M, Marsden BJ, Hall GN, Mummery PM, Graphite N. Keyway Root Crack Arrest in an Agr Graphite Brick. *23rd Int Conf Struct Mech React Technol*. 2015: 1–48.

24   Mostafavi M, Schmidt MJJ, Marsden BJ, Marrow TJ. Fracture behaviour of an anisotropic polygranular graphite (PGA). *Mater Sci Eng A*. 2012;558: 265–277.

25   Marrow TJ, Jordan MSL, Vertyagina Y. Towards a notch-sensitivity strength test for irradiated nuclear graphite structural integrity. *4th EDF Energy Nucl Graph Symp Eng Challenges Assoc with Life Graph React Cores*. 2014: 247–259.

26   Torabi AR. Sudden fracture from U-notches in fine-grained isostatic graphite under mixed mode I/II loading. *Int J Fract*. 2013;181: 309–316.

27   Torabi AR, Berto F. Strain energy density to assess mode II fracture in U-notched disk-type graphite plates. *Int J Damage Mech*. 2014;23: 917–930.

28   Ayatollahi MR, Berto F, Lazzarin P. Mixed mode brittle fracture of sharp and blunt V-notches in polycrystalline graphite. *Carbon N Y*. 2011;49: 2465–2474.

29   Berto F, Lazzarin P, Marangon C. Brittle fracture of U-notched graphite plates under mixed mode loading. *Mater Des*. 2012;41: 421–432.

30   Price RJ. Cyclic fatigue of near-isotropic graphite: Influence of stress cycle and neutron irradiation. *Carbon N Y*. 1978;16: 367–372.

31   Marshall P, Priddle EK. Room Temperature Fatigue Crack Propagation in Reactor Graphites. *Carbon N Y*. 1973;11: 541–546.

32   Kakui H, Oku T. Crack Growth Properties of Nuclear Graphite under Cyclic Loading Conditions. *J Nucl Mater*. 1986;137: 124–129.

33   Ishiyama S, Eto M. Effect of stress history on cumulative fatigue damage of fine-grained isotropic GCR graphite. *Carbon N Y*. 1996;34: 967–974.

34   Marsden BJ, Haverty M, Bodel W, et al. Dimensional change, irradiation creep and

17

thermal/mechanical property changes in nuclear graphite. *Int Mater Rev*. 2016;61: 155–182.

35   Jenkins GM. Analysis of the stress-strain relationships in reactor grade graphite. *Br J Appl Phys*. 1962;13: 30–32.

36   Fowell RJ. The chevron Notched Brazilian Disc Test Geometrical Considerations for Practical Rock Fracture Toughness Measurement. *Int J Rock Mech Min Sci Geomech Abstr*. 1993;30: 821–824.

37   Bay BK, Smith TS, Fyhrie DP, Saad M. Digital volume correlation: Three-dimensional strain mapping using X-ray tomography. *Exp Mech*. 1999;39: 217–226.

38   ABAQUS, Simulia Corp. Abaqus User's Guide. 2014.

39   Barhli SM, Mostafavi M, Cinar AF, Hollis D, Marrow TJ. J-Integral Calculation by Finite Element Processing of Measured Full-Field Surface Displacements. *Exp Mech*. 2017; DOI 10.1007/s11340-017-0275-1.

40   Bazant ZP. Concrete fracture models: testing and practice. Eng Fract Mech. 2002; 69:165-205.

41   Becker T, Marrow J. Modelling Damage in Nuclear Graphite. *13th Int Conf Fract*. 2013: 1–9.

42   Lubliner J, Oliver J, Oller S, Onate E. A Plastic-Damage Model for concrete. *Int J Solids Struct*. 1989;25: 299–326.

43   Ren W, Sneed LH, Yang Y, He R. Numerical simulation of prestressed precast concrete bridge deck panels using damage plasticity model, Int. J. Concr. Struct. Mater. 2015; 9: 45–54.

44.   Bompa D V., Elghazouli AY. Ultimate shear behaviour of hybrid reinforced concrete beam-to-steel column assemblages. *Eng Struct*. 2015;101: 318–336.

45   Tong J, Zhao LG, Lin B. Ratchetting strain as a driving force for fatigue crack growth. *Int J Fatigue*. 2013;46: 49–57.

46   Tong J, Lin B, Lu YW, et al. Near-tip strain evolution under cyclic loading: In situ

experimental observation and numerical modelling. *Int J Fatigue*. 2015;71: 45–52.

47   Zukas EG, O'Rourke JA, Armstrong PE, Green W V. The influence of creep strain on the elastic modulus, crystallographic orientation and density of a poco graphite. *Carbon N Y*. 1973;11.

48   Fazluddin S. Crack growth resistance in nuclear graphite. *PhD Thesis*. 2002.

49   Li Z. *Advanced Concrete Technology*. Hoboken, New Jersey: John Wiley & Sons; 2011.

50   Kim YJ, Kim HG, Im S. Mode decomposition of three-dimensional mixed-mode cracks via two-state integrals. *Int J Solids Struct*. 2001;38: 6405–6426.

51   Watanabe T, Tagata K, Yagawa G, Miyazaki N. J-integral analyses of plate and shell structures with through-wall cracks using thick shell elements. *Eng Fract Mech*. 1984;19: 1005–1012.

52   Maruyama T. Effect of Atmosphere on the Bend Strength of Nuclear Graphite. *Proc a Spec Meet held Tokai-mura, Japan*. 1991.

53   ASTM D7779-11. Standard Test Method for Determination of Fracture Toughness of Graphite at Ambient Temperature. *ASTM B Stand*. 2011;11: 1–9.

TABLE 1 Material parameters used in the damaged plasticity material model

Elastic Properties		Yield surface and Flow rule			
Young's modulus E(GPa)	Poisson's ratio υ	Dilation angle ψ	Eccentricity ϵ	Triaxiality ratio K_c	Viscosity parameter μ
11.9	0.21	30	4.8	0.667	0.0003

Tension softening		Tension damage		Compression damage	
Failure stress σ_{t0}(MPa)	Fracture energy G_f(J/m2)	Tensile damage d_t	Cracking disp u_t^{ck}(mm)	Compressive damage d_c	Inelastic strain $\tilde{\varepsilon}_c^{in}$
20	250	0	0	0	0
		0.99	0.025	0.99	0.045
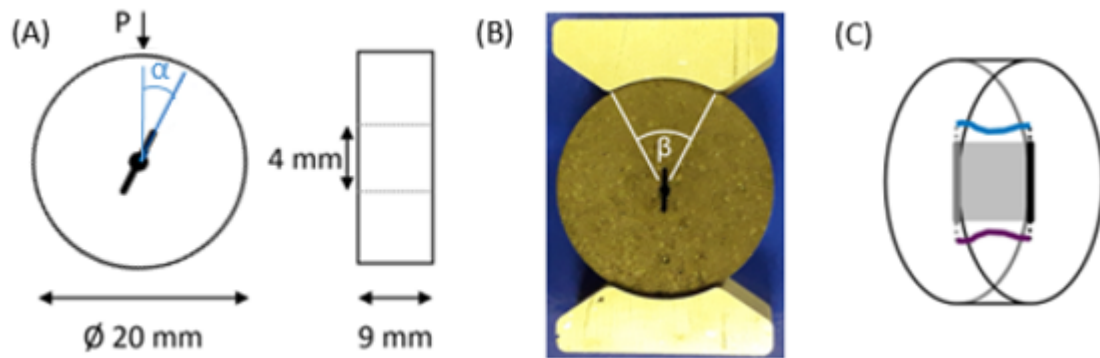
FIGURE 1 (A) An illustration of the Brazilian disk specimen tested at two loading angles α (0° and 27°); (B) the pre-cracking arrangement for the disk specimen. Two aluminium saddles were used to distribute the load over an area to avoid local damage to the edges of the specimen. The angle of the saddle contact area is β = 55°; (C) a schematic of the specimen with a machined notch (shaded area) and the crack geometries (coloured).
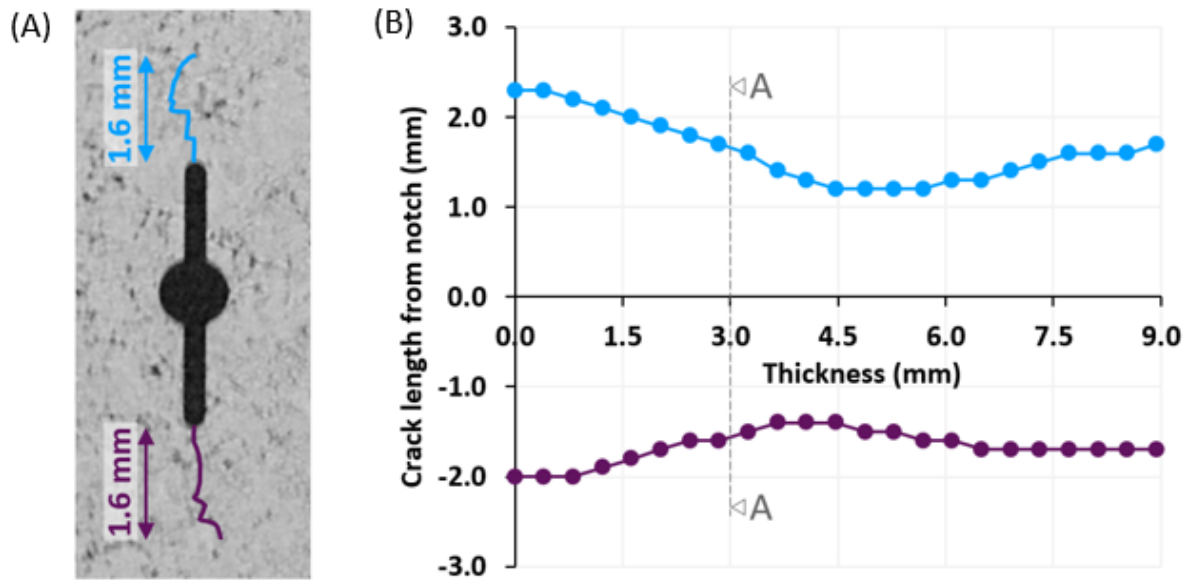
FIGURE 2 (A) The tomography image of the notch and the two cracks taken at section A-A as marked in (B), showing irregular crack paths; (B) The variation of the crack length across the thickness of the specimen measured from the tomographs. The crack lengths vary between 2.3 mm near the surface and 1.2 mm in the centre, with an average length about 1.6 mm.
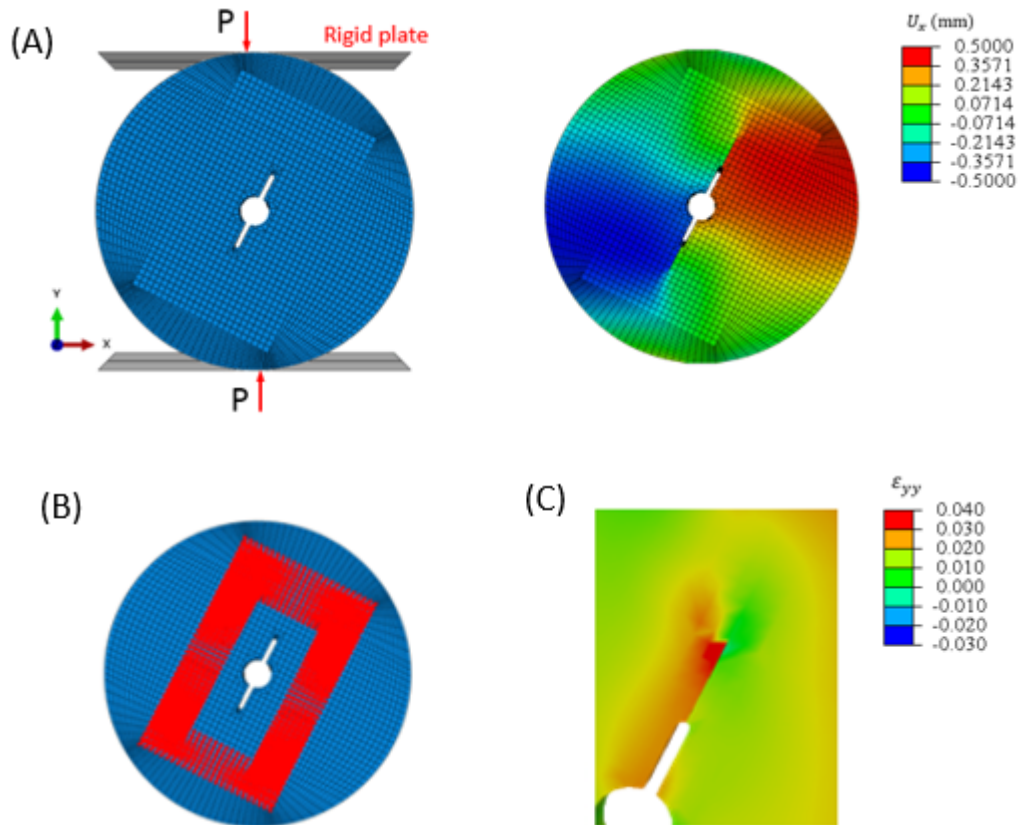
FIGURE 3 (A) The standard finite element (FE) model of the disk specimen loaded in compression applied through two rigid plates (left); and the corresponding displacement field (right); (B) the integrated FE model with the displacements (red) from the DVC introduced as the boundary conditions; (C) the strain ε_{yy} around the top crack computed from the model (B).
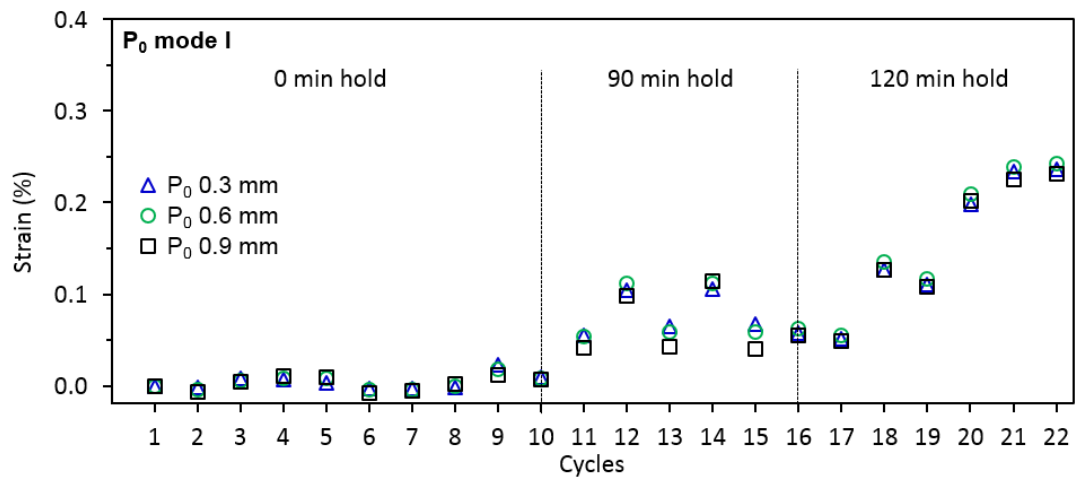
FIGURE 4 The accumulated normal strains measured at the minimum load P_0 post a hold period (0-120 mins) for the three mode I cyclic experiments. The strains were tracked at three positions ahead of the crack tip (blue: 0.3mm, green: 0.6mm and black: 0.9mm), with the reference taken at zero load prior to cycling.
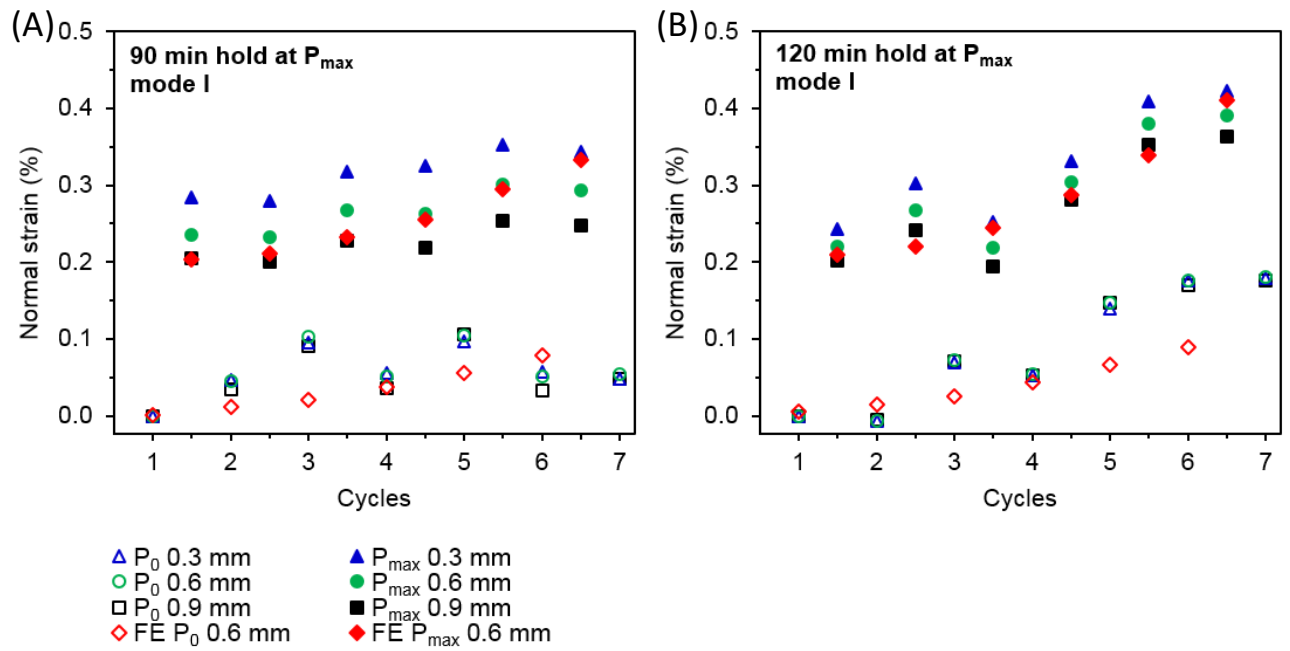
FIGURE 5 The evolution of normal strains during mode I cyclic loading during hold periods of (A) 90 minutes and (B) 120 minutes at the maximum P_{max} (closed symbols) and the minimum P_0 (open symbols) loads. The strains were tracked at three positions (blue: 0.3mm, green: 0.6mm and black: 0.9mm) ahead of the crack tip with the reference value taken at zero load. The results from the standard FE simulation (red: 0.6mm) are also included for comparison.
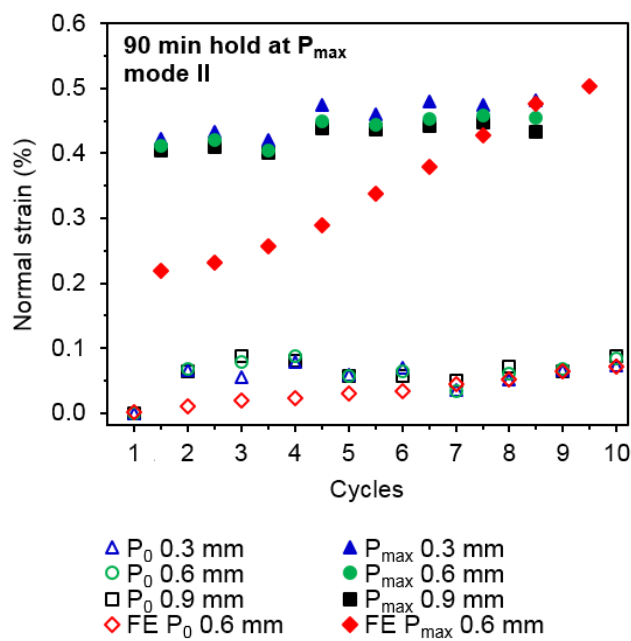
FIGURE 6 The evolution of shear strains during mode II loading post a hold period of 90 minutes at the maximum P_{max} (closed symbols) and the minimum P_0 (open symbols) loads. The strains were tracked at three positions ahead of the crack tip (blue: 0.3mm, green: 0.6mm and black: 0.9mm) and the reference value was taken at zero prior to cycling. The results from the standard FE simulation (red: 0.6mm) are also included for comparison.
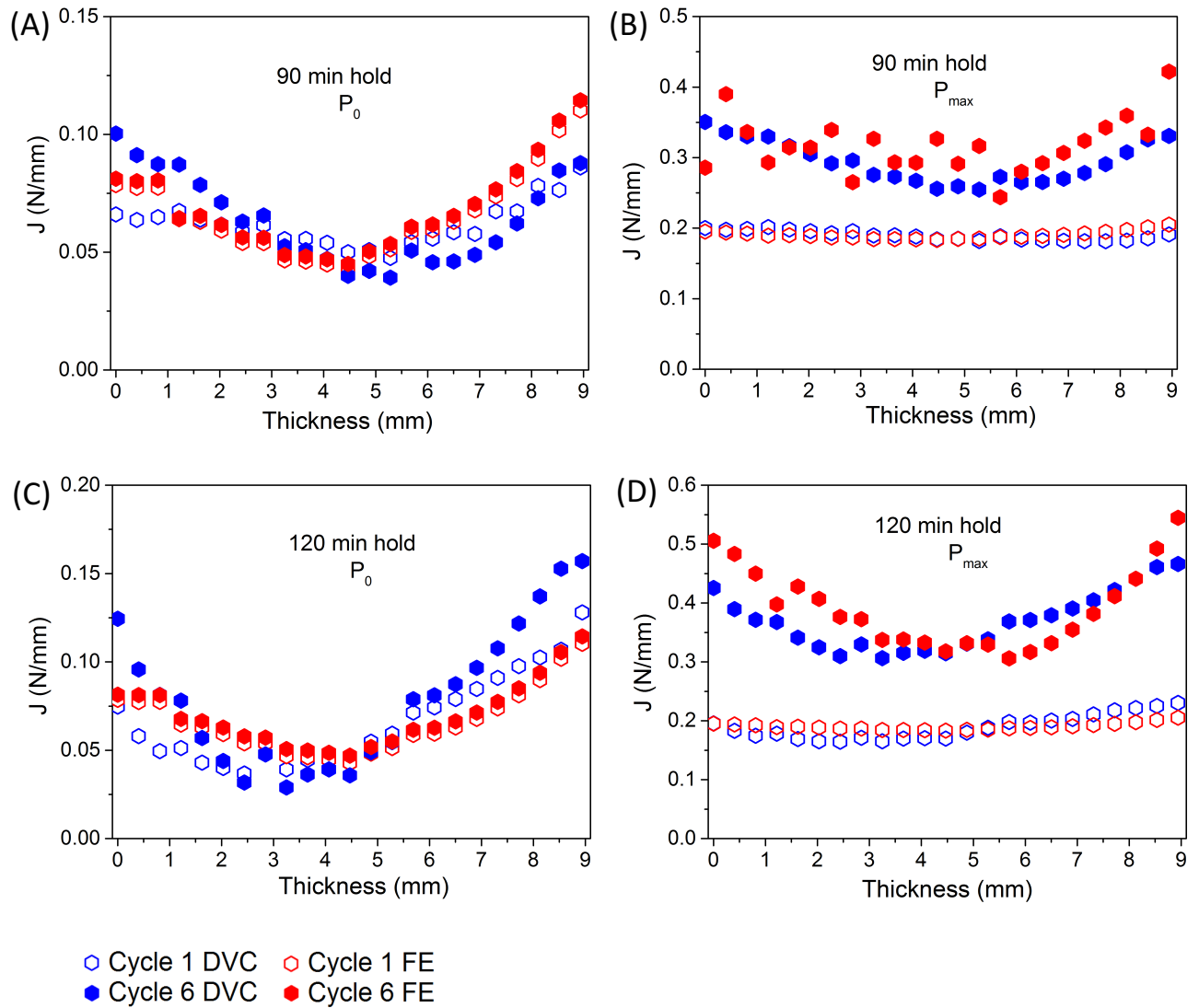
FIGURE 7 Comparison of the values of J-integral obtained from the integrated FE analysis (blue) and the standard FE analysis (red) along the crack front at Cycle 1 (open symbols) and Cycle 6 (closed symbols) at the minimum P_0 and the maximum P_{max} loads with a hold period of 90 minutes (A, B) and 120 minutes (C, D).
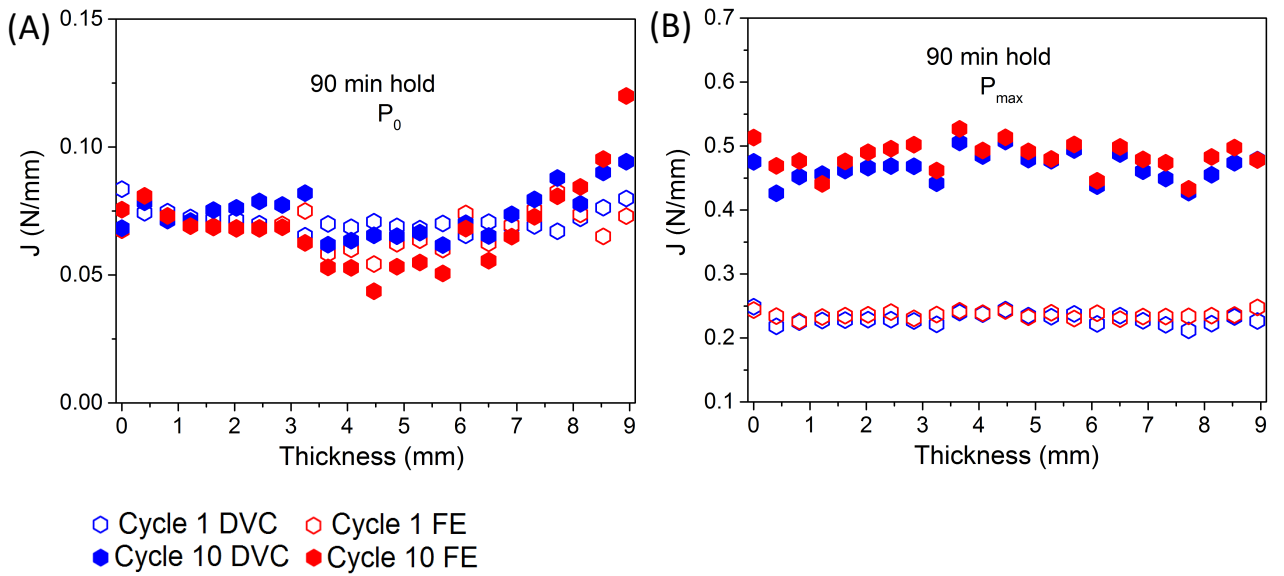
FIGURE 8 Comparison of the values of J-integral obtained from the integrated FE analysis (blue) and the standard FE analysis (red) along the crack front (top) at Cycle 1 (open symbols) and Cycle 10 (closed symbols) for mode II at the minimum P_0 and the maximum P_{max} loads with a hold period of 90 minutes.